Experimental Research on Rain-Induced Landslide Mechanism Using Large-Scale Rainfall Experimental Facility: Findings and Challenges

Naoki Sakai, Tomohiro Ishizawa, and Toru Danjo

Abstract

This paper presents the novel large-scale rainfall experimental facility, a pioneering development by the National Research Institute for Earth Science and Disaster Resilience (NIED). It delves into the intricacies of various large-scale slope failure experiments at this facility. These model experiments are unique in their approach, involving the attachment of multiple measuring instruments to a simple slope model. The standout feature of these experiments is the use of large-scale models, which facilitate easy handling of slope shaping, sensor placement, and application of realistic rainfalls, all tailored to the study's objectives.

The facility's unparalleled ability to control all experimental parameters is a crucial advantage, enabling the realization of more realistic natural rainfall conditions and external forces. This unique feature makes the experiments invaluable, setting our research apart. However, establishing diverse simulation methods is essential to exploit this advantage fully. The methods will allow us to explore a broader range of scenarios and further benefit from these experiments. While this study primarily discusses slope failure during rainfall, simulating post-collapse flow and transformation into debris flow is also necessary.

The experiments' findings shed light on the intimate relationship between groundwater levels and deformation, offering valuable insights into the collapse mechanism and its prediction. They also pinpoint the crucial points in preparing slope models, underscoring the practical implications of the research in controlling and mitigating slope failures.

Keywords

Large-scale model test · Heavy rainfall · Slope deformation · Experimental design

1 Introduction

Landslides and mudslides caused by typhoons, long spells of rain in June and September, and torrential rains brought on by training "linear precipitation zones" frequently occur in Japan, resulting in the yearly loss of precious human lives. It is reported that landslides account for about half of the total number of fatalities and missing persons in natural disasters. Landslide disasters remain among the most important natural disasters for which appropriate prevention measures should be taken.

In recent years, the Japan Meteorological Agency and prefectural and municipal governments have been issuing "landslide disaster warning information" and operating a system to support residents' evacuation and thus reduce landslide disasters. Precipitation is mainly used as an indicator, and information to provide warning guidelines is released in units of several-kilometer meshes or units of municipalities. On the other hand, the prediction of whether a particular slope is in danger of collapse is made using extensometers (e.g., Fukuzono 1985).

However, it is difficult to use this method as a warning that allows sufficient time for evacuation because surface failures occur very quickly after deformation begins. In the future, improving "landslide warning information" and establishing a field measurement method to evaluate the safety of specific slopes for the early prediction that goes one step beyond last-minute prediction will be necessary.

Figure 1 illustrates a shallow (1–2 m) slope failure in 2016 in Aso, Kumamoto Prefecture, Japan. The collapse directly above a structure and its impact on a building

N. Sakai (✉) · T. Ishizawa · T. Danjo
National Research Institute for Earth Science and Disaster Resilience (NIED), Storm, Flood and Landslide Research Division, Tsukuba, Ibaraki, Japan
e-mail: sakai@bosai.go.jp

B. Abolmasov et al. (eds.), *Progress in Landslide Research and Technology, Volume 3 Issue 2, 2024*, Progress in Landslide Research and Technology, https://doi.org/10.1007/978-3-031-72736-8_14

Fig. 1 Traces and residual soils left behind a debris flow (Aso, Kumamoto in 2016)

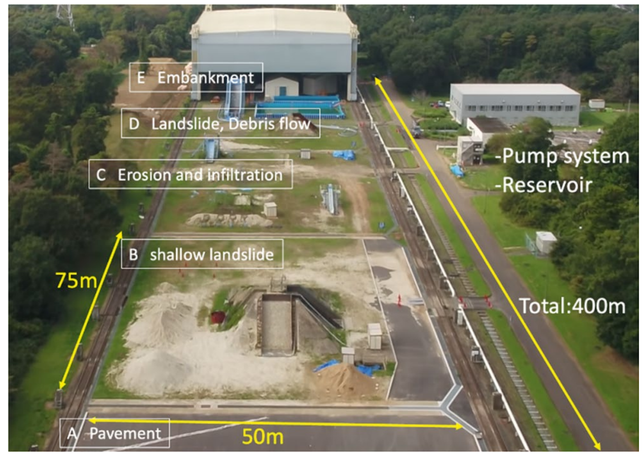

Fig. 2 Panoramic view of the large-scale rainfall experimental facility. Each of the five compartments has its own environment and facilities, and various experiments could be arranged based on the needs of the experiment

below was the result of a surface failure, believed to be a combination of factors including increased pore water pressure due to rainfall infiltration, decreased strength (apparent cohesion), and increased self-weight in the loose weathered layer above its bedrock. For a comprehensive understanding of these phenomena, it is crucial to comprehend the relationships among rainfall infiltration on unsaturated slopes, slope deformation associated with changes in saturation (Sasahara and Sakai 2014, 2017; Ishizawa et al. 2017), and slope deformation associated with the increase in the groundwater table. The authors have conducted field observations, developed analytical methods (Sasahara et al. 2007), and conducted experiments (Sakai and Sakajo 2008) on small slopes to develop a collapse prediction method considering the collapse mechanism. However, small model experiments have limitations in realizing the similarity law and are always different from the real ones (Moriwaki 1988). From this aspect, geotechnical centrifuge tests (e.g., Take et al. 2004) can be helpful for scale modeling of any large-scale nonlinear problem for which gravity is a primary driving force. However, even in centrifugal tests, shear-band development is geometrically determined by the representative soil grain size, which cannot be changed if we use natural sands as model materials. Therefore, large-scale model experiments utilizing the largest rainfall simulator are indispensable to minimize the problems associated with small model experiments and to gain a deeper understanding of slope failures (e.g., Moriwaki et al. 2004).

This paper illuminates the intimate relationship between groundwater levels and deformation, offering valuable insights into the collapse mechanism and its prediction. It also identifies the crucial points in preparing slope models, underscoring the research's practical implications for controlling and mitigating slope failures.

2 Large-Scale Rainfall Simulator

The National Research Institute for Earth Science and Disaster Resilience (NIED) developed a novel large-scale rainfall experimental facility in 1974 in Tsukuba, Ibaraki Prefecture, Japan. Figures 2 and 3 show the panoramic and indoor views of the Large-Scale Rainfall Experiment Facility. The compound (Fig. 3) comprises five experimental zones: a building with a mobile rainfall apparatus, a rainfall pump control building, and a water storage tank. Table 1 presents the rainfall performance of the facility. Among its various functions, the following three features are particularly noteworthy:

1. World's Largest Sprinkling Area:
   The facility can sprinkle water over a maximum indoor area of approximately 3000 m^2 ($\approx 44 \times 72$ m) using 2176 nozzles of four different types with varying spray diameters. Figure 3 shows the area is being sprinkled. This sizeable indoor area allows rainfall experiments using large-scale models close to the actual size. The sprinkling area can also be divided into four smaller sections, enabling multiple simultaneous rainfall experiments.
2. Mobile Rainfall Apparatus:
   The rainfall apparatus can move across five experimental zones on rails (shown in Fig. 2). The building can travel the most extended experimental zone (375 m) at a 1 m/min speed. This movable apparatus allows for the simultaneous execution of sprinkling experiments and model construction. Furthermore, comparative experiments can be conducted between natural and artificial rainfall conditions by moving the rainfall facility to expose the slope models to natural rainfall.

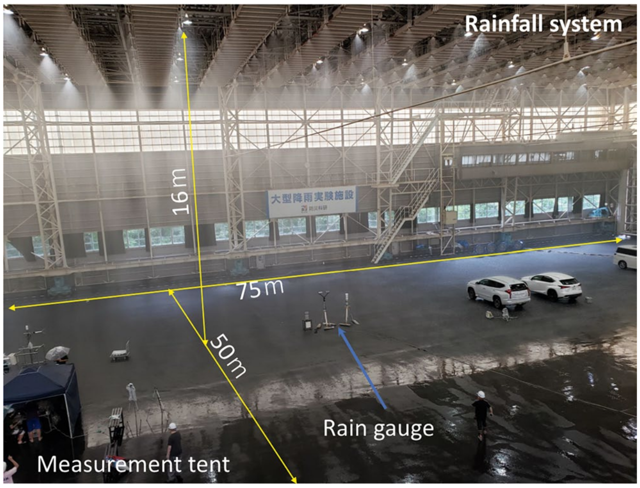

Fig. 3 Indoor view of the large-scale rainfall experimental facility

Table 1 Performance of the large-scale rainfall experimental facility

Large-scale mobile rainfall facility	
Structure (area)	Steel-pipe-trussed ferroconcrete (3492 m^2)
Observation room	Floor 7.5 m above the ground
	2 rooms of 65.4 m^2 each
Sprinkling area	50 × 75 m, 5 divisions
Sprinkling facility	
Raindrop size	0.1–8 mm diameter (4 type nozzles)
Rainfall intensity	15–300 mm/h
Rainfall area	50 × 75 m (dividable into quarters)
Nozzles	System 1:15–45 mm/h 544 pcs.
	System 2:40–200 mm/h 544 pcs.
	System 3:120–220 mm/h 544 pcs.
	System 4:200–300 mm/h 544 pcs.
Nozzle height	16 m above the ground
Control	Remote control: flow rate/stress control
Circulating pump	200 kW, 9.4 kg/cm^2, 8.0 kl/min, 2 pumps
Reservoir	
Water storage capacity	2500 m^3
Supply well	80 m^3/h

3. The facility's ability to replicate heavy and sudden downpours is a significant feature that adds a sense of realism and practicality to the research:

The facility can simulate rainfall intensities from a minimum of 15 mm/h to 300 mm/h, with raindrop sizes up to about 8 mm. Experiments can replicate the maximum hourly rainfall recorded in Japan, such as 187.0 mm/h observed in Nagayo Town, Nagasaki in July 1982, and 50.0 mm in 10 min in Murakami, Aga Town, Niigata Prefecture, on July 26, 2011.

Following overhauling the sprinkling system in 2014, the facility enhanced its capability to simulate rainfall intensities up to 300 mm/h, like sudden downpours. It can replicate

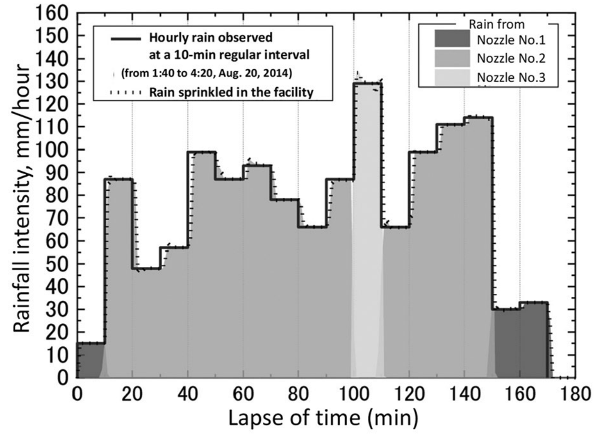

Fig. 4 Rain gauge record in Hiroshima, 2014 and the realized rain sprinkled in the facility

continuous rainfall conditions with varying intensities, similar to actual rainfall. To verify the sprinkling performance, we reproduced the localized short-duration heavy rain that caused significant damage, such as landslides and floods in Hiroshima during the heavy rain event in August 2014. Figure 4 shows the results of this reproduction. The solid line in the Figure represents the record retrieved from the Automated Meteorological Data Acquisition System (AMeDAS) observation point in Miiro, Hiroshima Prefecture. The broken line shows the 10-min interval sprinkling results reproduced by the facility. The experiment used different nozzles to change the rain intensity every 10 min and accurately reproduce the observed short-duration rainfall. The excellent agreement between the observed and realized rains showed the satisfactory performance of the sprinkling system.

3 Large-Scale Model Slope Experiments in Artificial Rainfalls

In a large-scale model test, it is essential to record the slope failure process to foresee the risk of failure, which is almost impossible on natural slopes. We measured the following processes in the experiments to see how they would develop until the slope started sliding:

1. the saturation process due to rainfall infiltration
2. the change in the groundwater level
3. the ground surface displacements

3.1 Preparations

Each model was prepared in a composite steel soil bin (Figs. 5 and 6) for a total slope length of 23 m (including a 10 m and

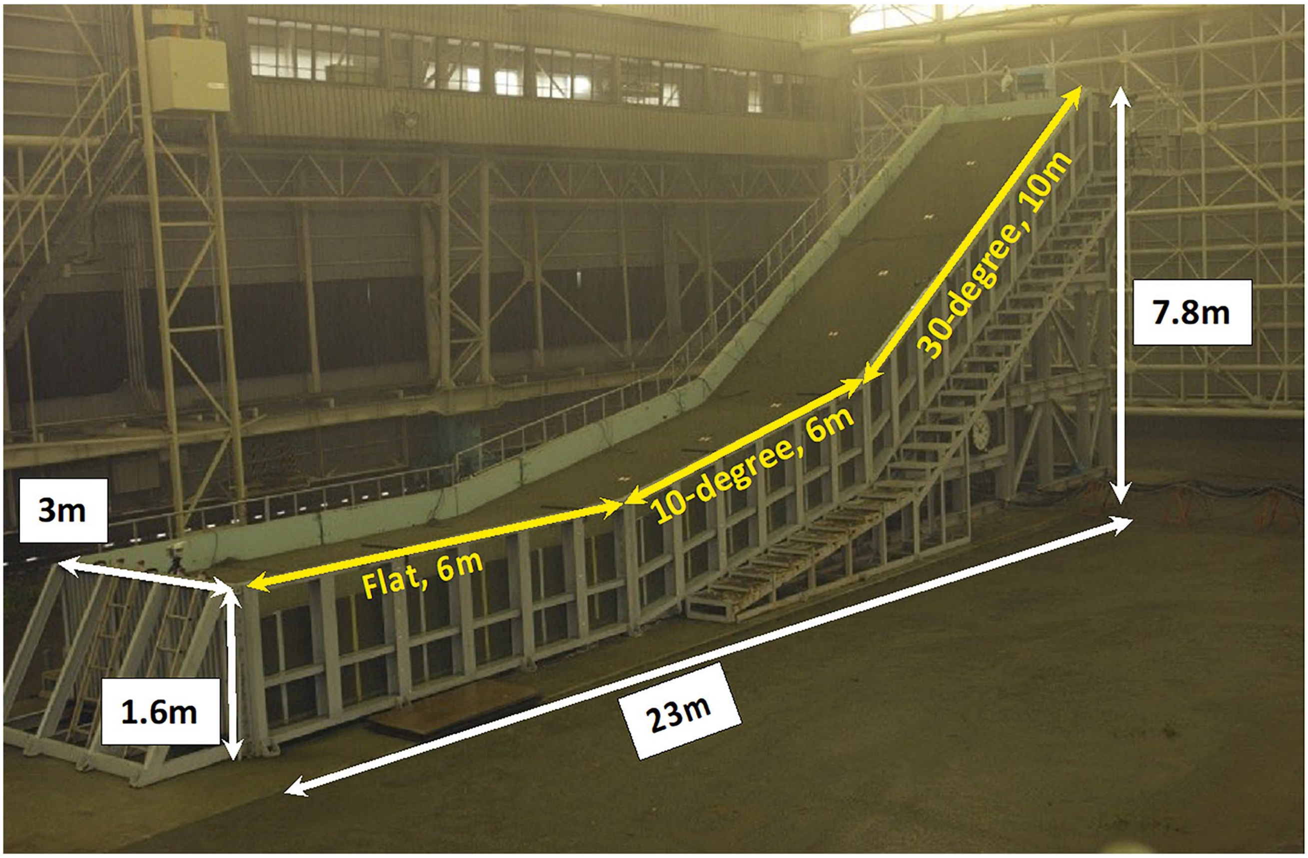

Fig. 5 Composite steel soil bin

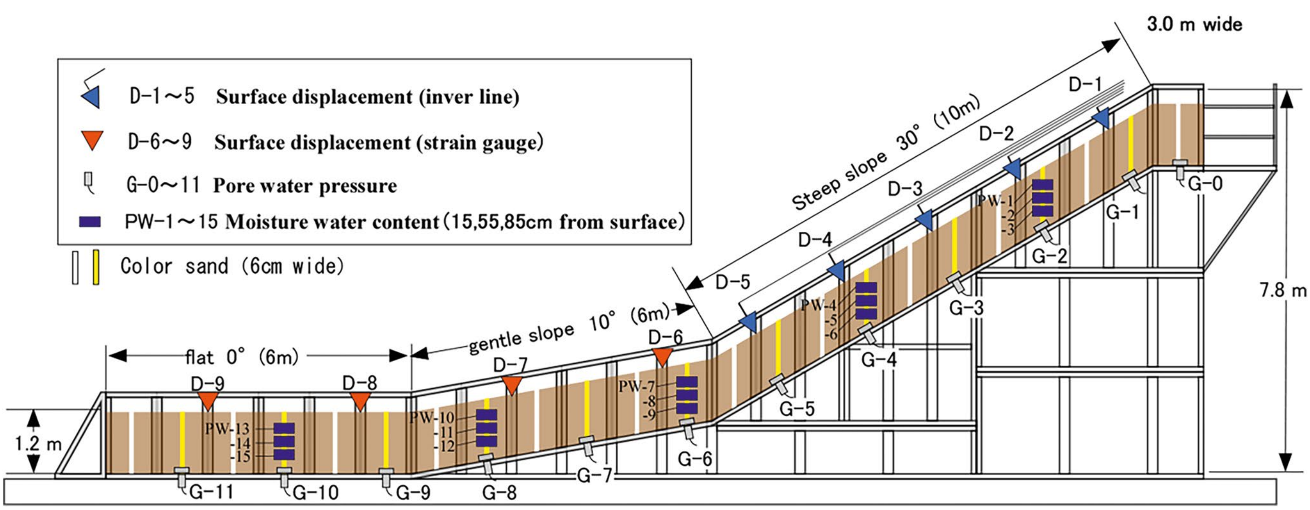

Fig. 6 Arrangement of sensors

30° slope section), 3 m wide, 1.6 m deep (soil layer depth: 1.2 m), and 7.8 m high at the upper end. The lower end of the soil bin is a slit-type retaining wall sealed with a wire mesh, allowing the water in the model to drain through the slits while retaining the soil within the soil bin (Fig. 7). The other sides of the soil bin are entirely impermeable. Cleats are arranged horizontally on the bottom of the slope at regular intervals to stop the soil from sliding. The light walls from the face of the soil bin are glass-paned so that the deforming process of the soil layer can be observed from the outside. The slope model of sand with an initial moisture content of about 8% was compacted manually at every 20 cm thickness (Fig. 8). The prepared slope model's average dry density and pore ratios were 1.37 g/cm^3 and 0.964, respectively.

Fig. 7 Lower end of the soil bin (Slit-type retaining wall sealed with a wire mesh)

Fig. 8 Compacting the slope soil (image)

Surface displacement gauges (D1–D9), soil moisture gauges (PW1–PW15), and pore pressure gauges (G0-11) were installed, as shown in Fig. 6. The surface displacement gauges from D1 to D5 are wire extensometers with their wires' lower ends fixed on the predetermined locations of the slope model's surface with four-legged weights. The other end of each wire with a counterweight hangs down over a pulley of its potentiometer above the top end of the steel soil bin (Fig. 9). The counterweight ensures tension on the wire. D6 to D9 are vertical displacement sensors (Figs. 10 and 11). Each sensor is a cantilever of phosphor bronze with strain gauges pasted; the cantilever is placed immediately above the slope surface. A rigid probe tip attached at the free end of the cantilever is pressed down to a target steel plate placed on the surface of the slope model in such a way that the cantilever is bent upward as its initial condition, thus allowing the vertical displacement of the target plate to be measured until the stress induced in the cantilever is ultimately released.

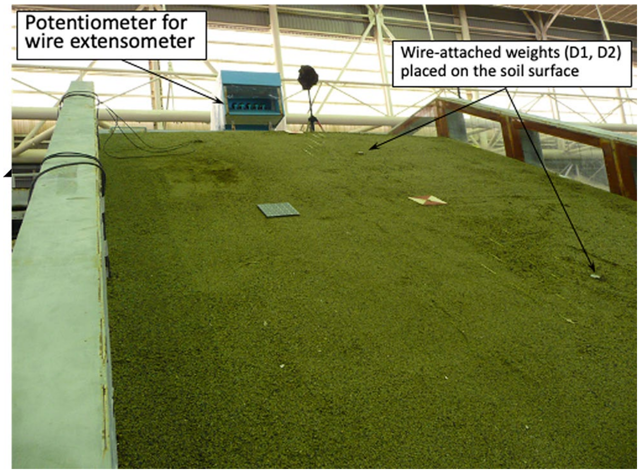

Fig. 9 Potentiometers for wire extensometers (D1–D5) at the top end of the slope model

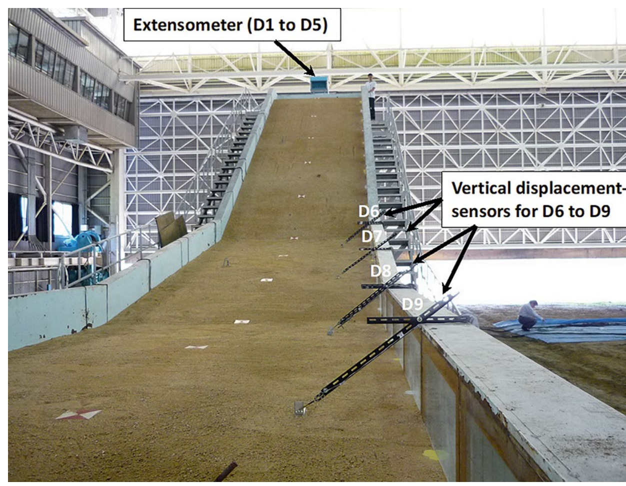

Fig. 10 Extensometer for D1 to D5 and vertical displacement sensors for D6 to D9

Fig. 11 Cantilevers of phosphor bronze with strain gauges pasted: Each cantilever with a rigid probe tip is attached at one end of a steel support. The rigid tip is pressed down to a target plate placed on the surface of the slope model

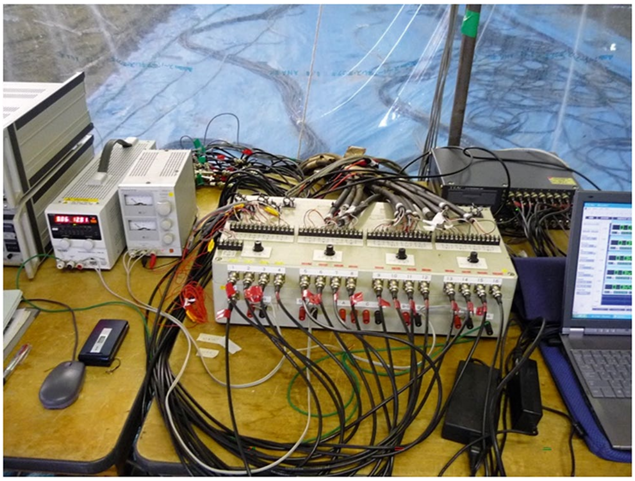

Fig. 12 A signal processing system with dozens of channels

Fig. 13 Data acquisition in a tent

Amplitude Domain Reflectometry (ADR) soil moisture sensors were placed at 15 cm, 55 cm, and 85 cm from the slope surface to measure volumetric moisture contents. Groundwater distribution in the soil layer was calculated from pore water pressures measured at the bottom of the soil bin. The analog signals from the sensors were transferred to a data logger and converted to digital signals every 10 s to be stored in it. The digital signals can be transferred to a computer for further signal processing (Fig. 12).

Though the experiment was conducted indoors, the area was vast and wet, with simulated rains. Therefore, the experiments required a measurement tent (Fig. 13) on the right side of Fig. 5.

Commercially available Sawara sand, classified as gravelly sand, was used to make slope models in all experiments. The uniformity coefficient (Uc) and the diameter corresponding to 20% finer in the particle-size distribution (D20) of the Sawara sand are 3.689 and 0.2284, respectively. Figure 14 shows the cumulative grain-size distribution curve of the Sawara sand. The soil's particle density and saturated permeability are 2.690 g/cm^3 and 2.71 × 10^{-2} (cm/s), respectively.

In addition, a water retention test (multi-step test apparatus) was conducted to determine the ability of the Sawara sand to retain water under suction (Fig. 15). The obtained results show the relationship between suction and saturation degree. The soil specimen was cylindrical, 5 cm in diameter, and 5 cm high. Its dry density was measured in the soil tank. The test methods used were the hydraulic head difference and pressurization methods. The first step of drying was then followed by wetting. The observed hysteresis was weak. This sample's AEV (Air Entry Value) pressure was about several kPa, similar to that of ordinary sand.

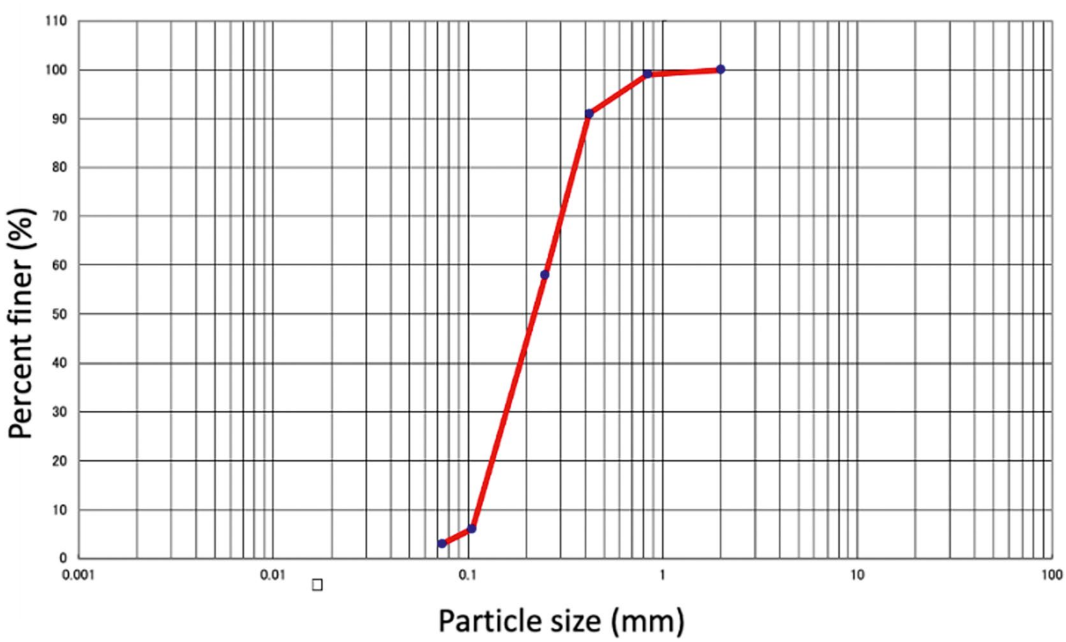

Fig. 14 The cumulative grain-size distribution curve of the Sawara sand

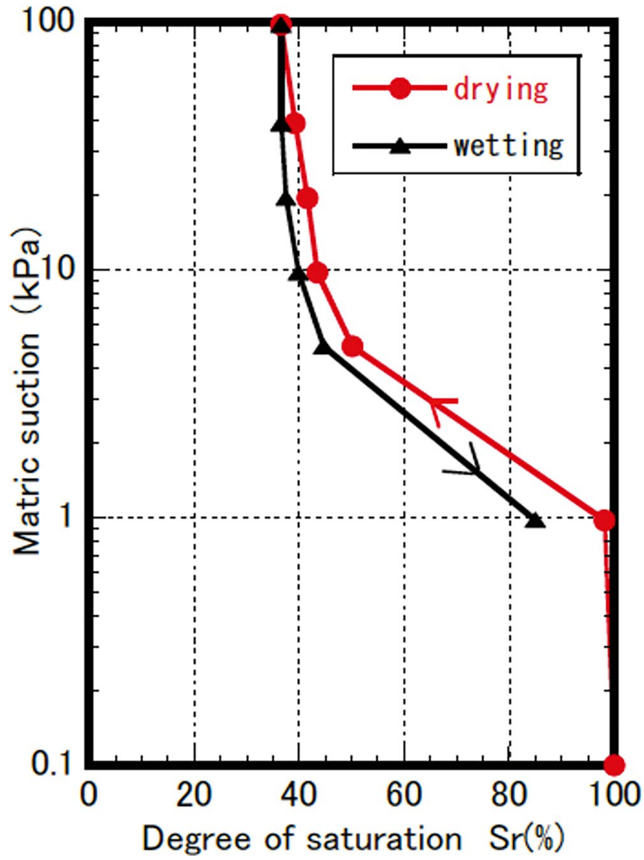

Fig. 15 Water retention curve for Sawara sand

4 Groundwater Formation Processes in the Slopes due to Rainfall

4.1 Case 1 with No Prior Rainfall to the Main Rainfall Event

Under these initial conditions, a steady 100 mm/h rain was continuously given to the model's surface until it collapsed (t = 8515 s, i.e., 2 h and 23 min, Table 2). The soil moisture meters (PW-4, 5, and 6) installed along the bottom of the slope in Fig. 16 showed that the saturation degrees continued to rise from the upper part to the lower parts of the slope (PW-4, PW-5, and PW-6 at around 900 s, 2200 s, and 4500 s, respectively) from their initial values below 40%. These values then converged at their steady state of about 70–80%. This steady state is the pseudo-saturation that appears when a wetting front passes through the location. Later, the complete saturation levels (100%) were reached at PW-6 and then at PW-5 immediately before the collapse time.

Figure 17 shows the chronological changes (t = 3000 to 9000 s) in the groundwater levels measured at five pore pressure gauges from G1 through G5 placed on the bottom of the 30-degree section of the soil bin. At t = 6400 s, G1 and G5 started rising, followed by increases in G2 and G3 (at t = 6800 s) and finally G4 (at t = 7100 s). G1 through G4 increase to conform with each other, while G5 near the lower end of the 30-degree slope shows slightly more significant values. This tendency suggests that the groundwater level was increasing almost parallel to the bottom of the soil bin. Upright broken lines (1), (2), (3), and (4) in Fig. 16, 17, and 18 show 10, 20, and 30 min before the slope collapse time. These times cover the later phase of the experiment, where the groundwater level started to increase. Figure 18 shows that even before 40 min of the collapse, the soil mass on the 30-degree section started to move downslope coherently. At 40 min and later before the collapse, D5, placed at the lower end of the 30-degree section, moved further away from the others. Connecting the estimated groundwater levels (G0 through G11), we obtained the spatial variations of the groundwater levels over the entire model stretch at different times, as shown in Fig. 19. Until 30 min before the entire collapse, the groundwater level (Line (4)) increased remarkably only in the flat toe part and the gentle slope part; this process did not seem to have initiated the downslope movement of the upper 30-degree slope section. After this time, the groundwater level within the 30-degree slope section started to rise, accelerating the downslope creeping mass movement, which developed as shown in Fig. 18. It is noteworthy that this process resembles the final stage of a natural landslide mass movement comprising the initial transient, intermediate steady, and the final accelerating creep processes.

4.2 Case 2 with Prior Rainfalls to the Main Rainfall Event

The slope model in Case 2 was prepared in the same soil bin in the same manner as in Case 1. Then, four intermittent rains were sprinkled before the main torrential 100 mm/h rain, which continued until the entire slope collapsed, as in Case 1 (Table 3). The intention was to see the effect of the preceding four rains on the soil deformation process, which is associated with the water infiltration into the soil model.

Figures 20 and 21 show the chronological changes in saturation and groundwater level, respectively. Both Figures have secondary axes going downward, showing the rainfall intensities of the preceding four rainfalls (30 mm/h) and the actual rainfall (100 mm/h) shown as blue downward bars.

Immediately after the first preceding 4-h rain of 30 mm/h, the groundwater levels at G-3, G-4, and G-5 showed steady increases, surpassing the others at G-1 and G-2. G-3 reached its peak of about 10 cm, and then G-4 and G-5 followed it, reaching slightly higher values (15 cm and 18 cm) one by one. The G-3 peak value appeared about 2 h after the first rain stopped. These groundwater levels then gradually decreased exponentially.

Table 2 Case 1 test condition for rainfall

Rain event	Time before start	Rainfall intensity (mm/h)	Duration (h)	Total rainfall (mm)
Main event	0 day and 0 h	100	2.37 (8515 s)	237 mm

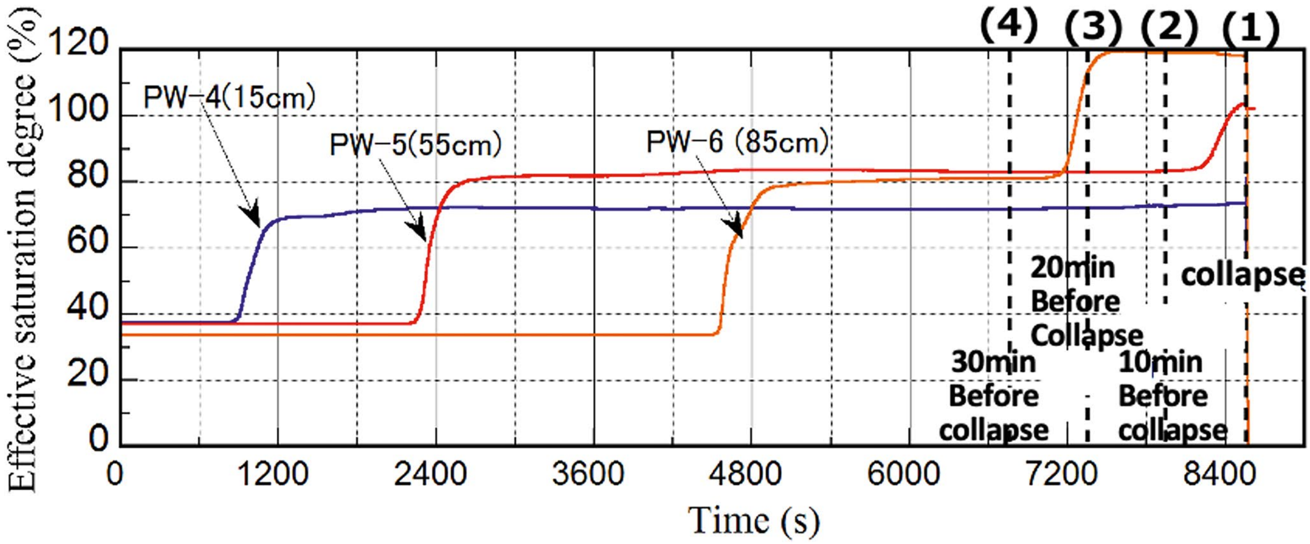

Fig. 16 Chronological changes in saturation degrees (PW-4 to PW-6)

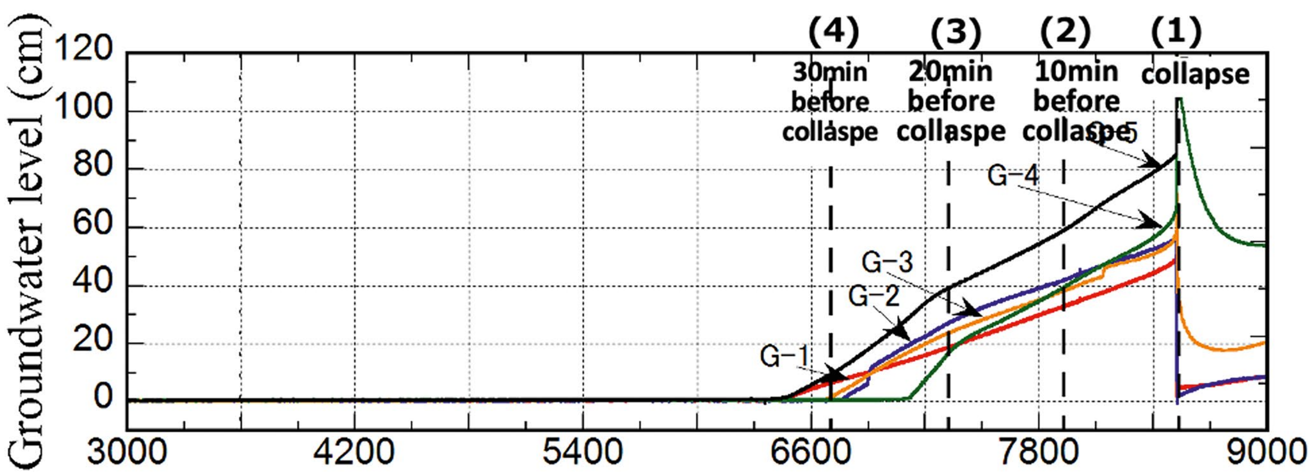

Fig. 17 Chronological changes in groundwater levels (G-1 to G-5)

The second preceding rain of 30 mm/h lasted 3 h. Though the time was shorter than that of the first rain, the peak values reached by G-3, G-4, and G-5 were more significant than 20 mm, suggesting the impact of the first rain.

All moisture gauges show a common trend: the saturation degrees exhibited exponential decaying responses to rainfall. On the other hand, the groundwater levels peaked a few hours after the end of each rainfall event. In all cases, the increase in the water level was faster and predominant in the middle to lower part of the slope (G-3, 4, 5), while they were less significant in the upper part (G-2, 1). This feature suggests groundwater flows from the top to the bottom of the slope. Thus, the groundwater level never becomes parallel to the slope surface but gentler than that, making its depth larger as we go upward. The groundwater-level signals from G-3, G-4, and G-5 went below zero as the groundwater drained, as shown in Fig. 21, due to the suction associated with the interparticle surface tension that appears in the drainage process.

The surface displacement gauges, D1 through D5, placed on the surface of the 30-degree slope section, showed simultaneous stepwise increases (less than 1 cm) immediately after the first rainfall event (1) (Fig. 22). The

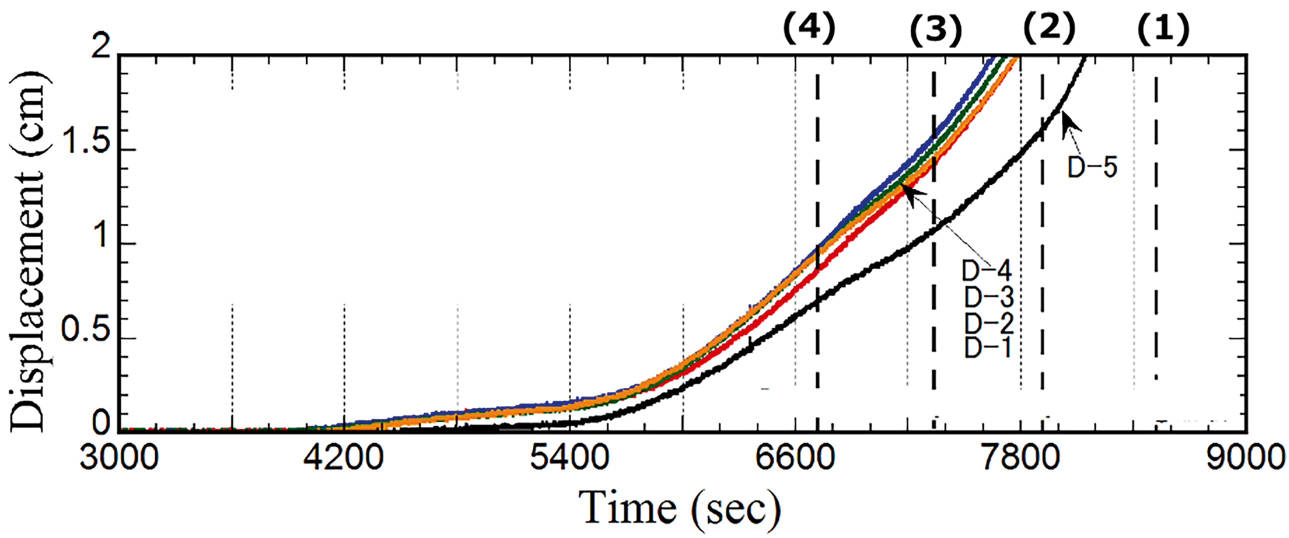

Fig. 18 Downslope movements, D1 to D5, placed over the 30-degree slope section

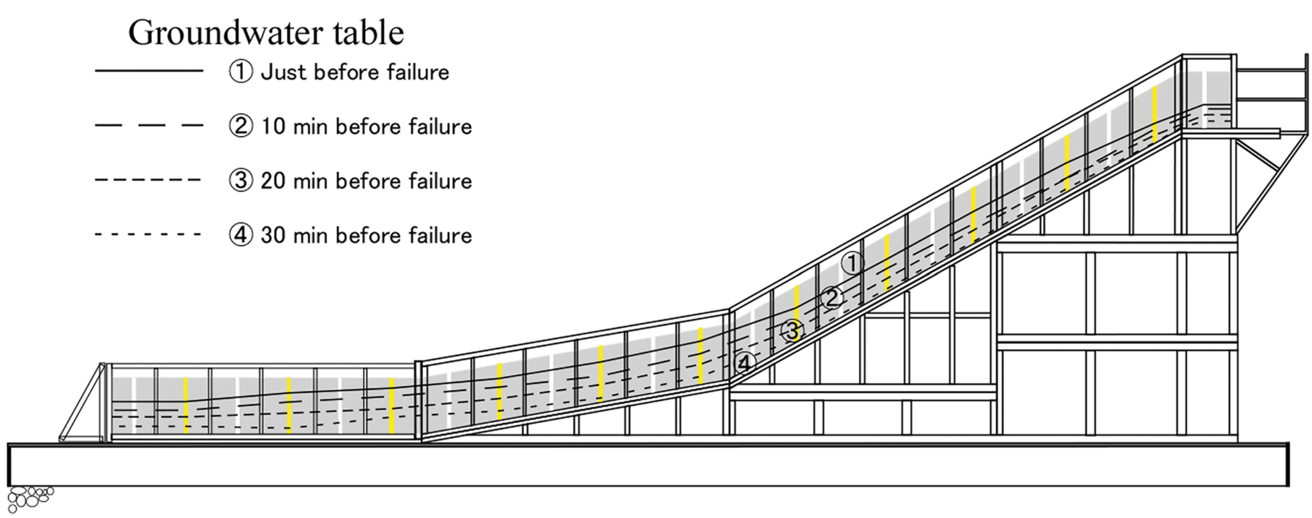

Fig. 19 Chronological change in the groundwater table in Case 1

Table 3 Preceding rains and the main torrential 100 mm/h rain

Rain event	Time before start	Rainfall intensity (mm/h)	Duration (h)	Total rainfall (mm)
Preceding event No. 1	0 day and 0 h	30	4	120
Preceding event No. 2	1 days and 22 h	30	3	90
Preceding event No. 3	3 days and 1 h	30	2	60
Preceding event No. 4	5 days and 22 h	30	3	90
Main event	7 days and 1 h	100	1.69 (6082 s)	168

displacements then gradually increased in small stages on the order of mm. However, no obvious relation was found between the rains that followed the first one and the small changes in the displacements. Though minor, these small deformations of the slope model (particularly in the first rain) can cause transverse cracks to appear, as shown in Fig. 23.

These preceding rains never increased the groundwater level in the 30-degree slope section. Thus, the slope model's main "30-degree" section remained stable. However, the groundwater level increased in the flat toe part and the gentle 10-degree sections from the bottom of the soil bin to the thick broken line in Fig. 24. The rains also increased the average saturation ratio from below 40 % to over 45 %.

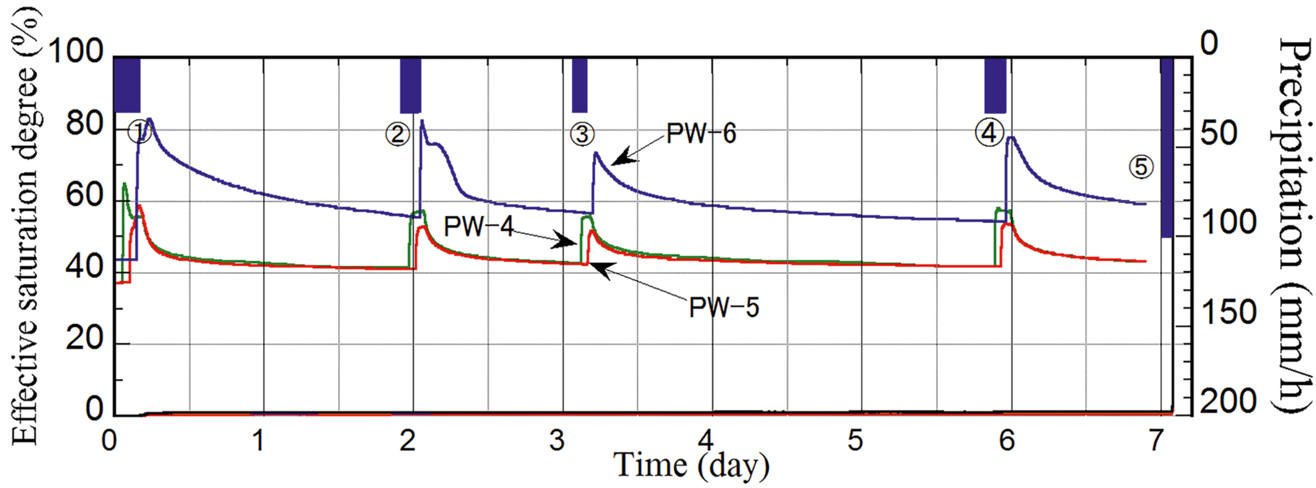

Fig. 20 Chronological changes in saturation degrees and preceding rains

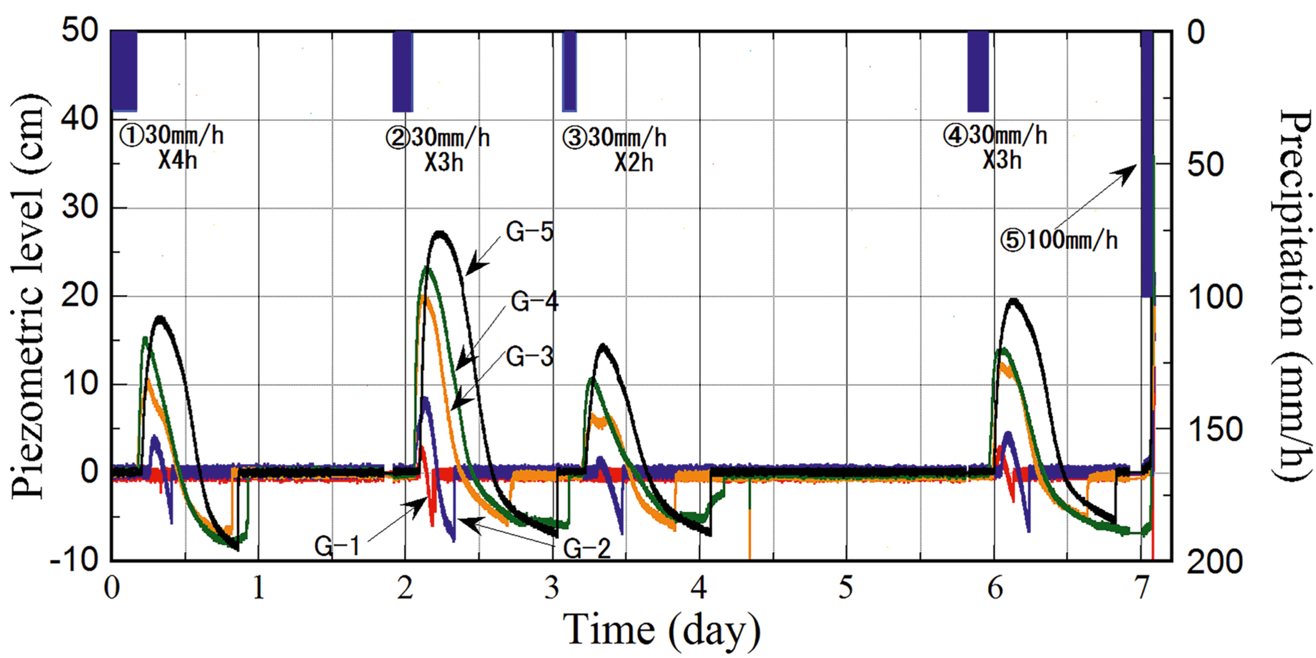

Fig. 21 Chronological changes in groundwater levels and preceding rains

Given the above hydraulic condition as the initial condition, torrential 100 mm/h rain was continuously sprinkled on the slope model's surface, as we did in Case 1.

Figure 25 shows the chronological changes (t = 0 to 6000 s) in the groundwater levels measured at five pore pressure gauges from G1 through G5 placed on the bottom of the 30-degree section of the soil bin. Upright broken lines (1), (2), (3), and (4) in Figs. 25 and 26 show times 10, 20, 30, and 40 min before the slope collapse time. G5 and G4 started to rise at around t = 4200 s (about 40 min before the collapse (4)), which was followed by the increase in G3 at around t = 4500 s, and then G2 and G1 at around t = 4900 s. In short, the groundwater level started to rise sequentially from the lower to the upper parts of the 30-degree section. The upper frontal end of the zone, where the groundwater seeps out from the model's surface, gradually moved up until it reached the lower end of the 30-degree section 10 min before the collapse (1). At this time (1), the groundwater at the top end of the 30-degree section was about 40 cm deep. Then, the whole collapse occurred in 10 min.

Figure 26 shows that the soil mass (D5 to D2) on the 30-degree section started to move coherently downslope at around t = 4900 s. The displacement buildup at D1 (started at t = 5100 s) followed these movements. These displacement buildups were gradually accelerated until the entire slope collapsed. Compared with Fig. 18, the downslope movement

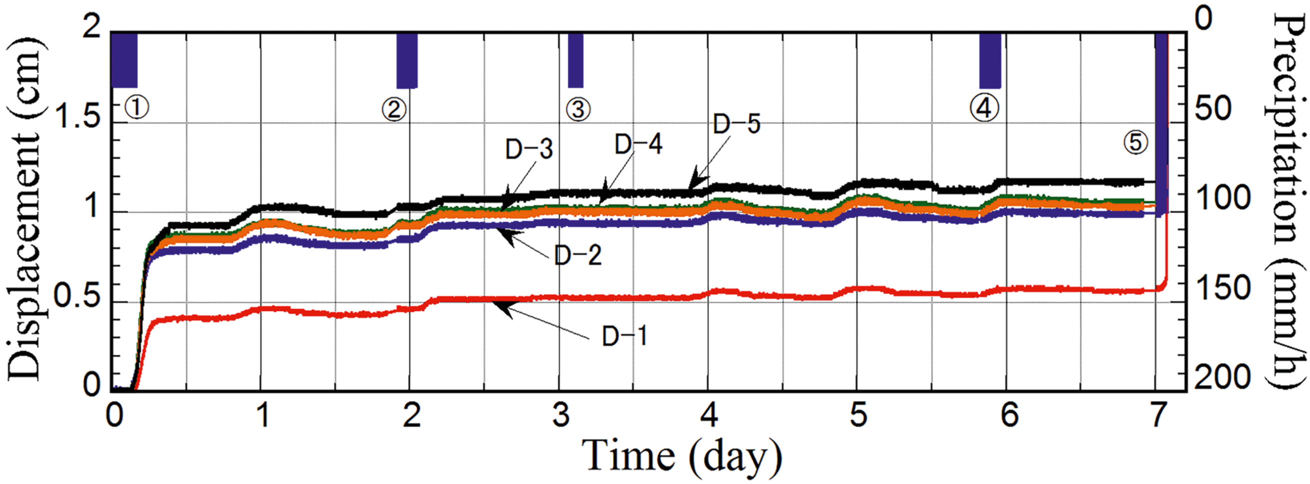

Fig. 22 Chronological changes in downslope displacements (D1 to D5) and preceding rains

Fig. 23 Transverse cracks that appeared near the top end of the 30-degree slope section immediately after the preceding rain No. 1

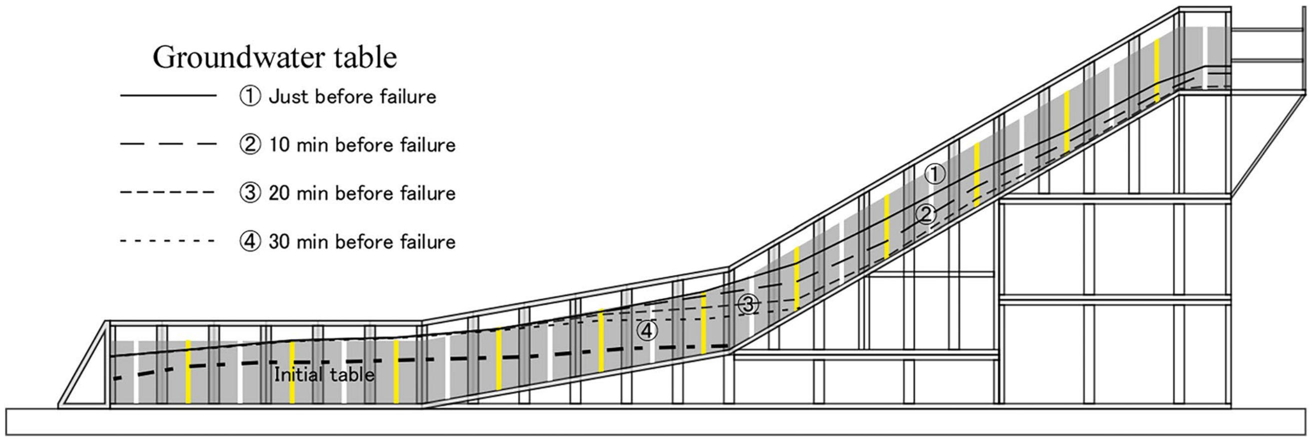

Fig. 24 Chronological change in the groundwater table in Case 2

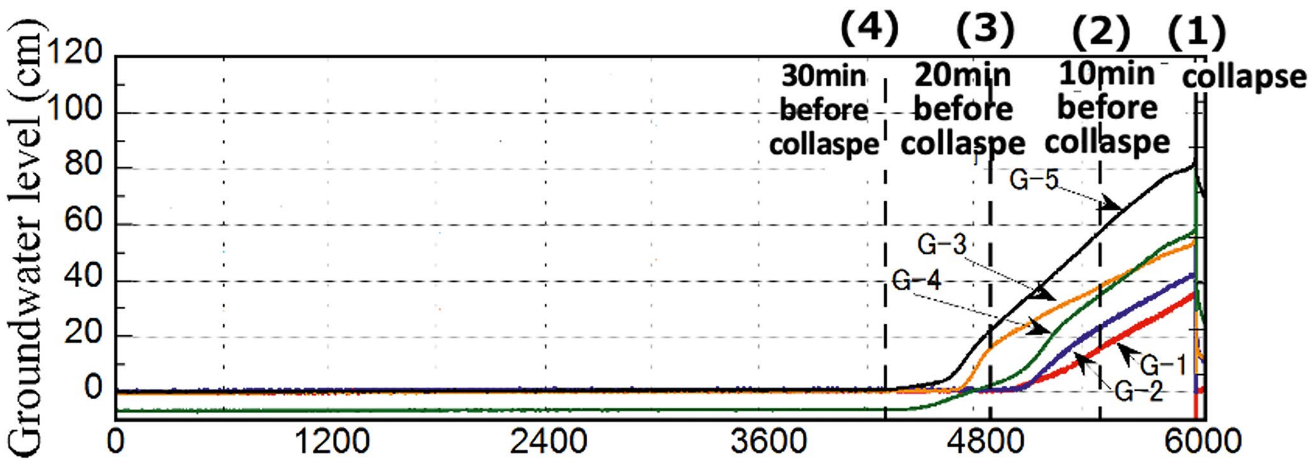

Fig. 25 Chronological changes in groundwater levels (G-1 to G-5, Case 2)

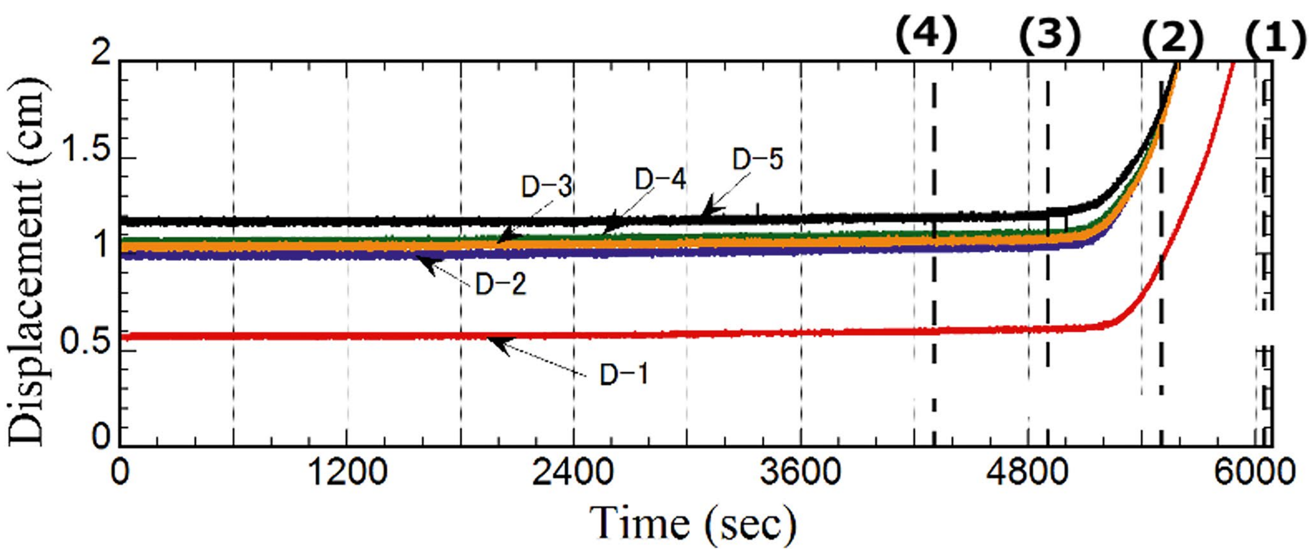

Fig. 26 Downslope movements, D1 to D5, placed over the 30-degree slope section (Case 2)

of the wet soil mass in Case 2 was much faster than in Case 1, reflecting the faster increase in the groundwater level.

5 Slope Deformation Processes due to Heavy Rainfall

The most important feature of this large-scale experiment is that it allows us to directly see the deformation in the slope ground.

In general, it is difficult to clarify the process from deformation to failure in model experiments due to the effects of scale and friction on the circumference.

However, in this large model experiment, the effect mentioned above is minimized because the experiment is conducted on a realistic scale.

The results will be particularly useful for simulation studies of rainfall infiltration and deformation.

This section describes the methodology used to achieve this.

The steel frame for the large model experiment is 23 m in length and is divided into sections.

The top of the slope is 1 m long, the 30-degree slope 10 m long, the 10-degree slope 6 m long, and the flat section 6 m long, each containing a steel frame every 1 m, with reinforced glass in between the frames.

The slope deformation indicator is completed by setting white sand bars between the frames.

Here, numbers (c0–c22) are written on the white sand columns to make it easier to track the changes (see Fig. 27).

As explained earlier, the soil bin's glass-paned side walls allow easy observation of the soil layer's deforming process from the outside (Fig. 27). Though the soil models prepared in Cases 1 and 2 were the same as each other, the slip surfaces that developed in the interiors of these soil models differed, as will be explained herein, reflecting the absence (Case 1) and presence (Case 2) of the pre-wetting processes.

For easy observation of the deforming process, the soil models in Case 1 and Case 2 had white-colored sand columns embedded at regular intervals along the glass-paned wall (Fig. 28). Since each glass-paned side wall has upright stiffeners arranged at regular intervals of 1 m to stiffen the wall against out-of-plane deformations, sand bars were evenly arranged between each pair of the neighboring stiffeners. The following processes made each sand column:

1. filling a plastic half-cylindrical 8 cm-mold with white sand,
2. putting the mold on the glass pane of the soil bin,
3. filling the soil bin with sand to make the slope model, and finally
4. pulling the mold out of the slope model.

5.1 Case 1 with no Prior Rainfall to the Main Rainfall Event

As detailed earlier, the model's collapse occurred precisely 8,515 seconds after the onset of continuous 100 mm/s rainfall. The entire collapse transpired within the final 5 seconds. Fig. 29 presents the last 3-second sequence, providing a frame-by-frame progression (at every 1-second interval) of the slope's ultimate collapse. This process is characterized by the model's surface cracking and bulging at its top and toe parts, as depicted in Fig. 30. The frame-by-frame collapse progression (5 frames at every 1/6-second interval) in Fig. 31 illustrates the development of the slip surface within the 30-degree slope section with meticulous detail.

In (1) of Fig. 29, columns c1 to c9 are tilted forward.

The yellow dotted line drawn in Fig. 29 (2) connects bends and kinks observed in white sand columns c1 through c10, thus showing the deduced slip surface developed over the 30-degree slope section. Sand columns from c3 to c7 faded due to this part's extensive downslope movement. The sand

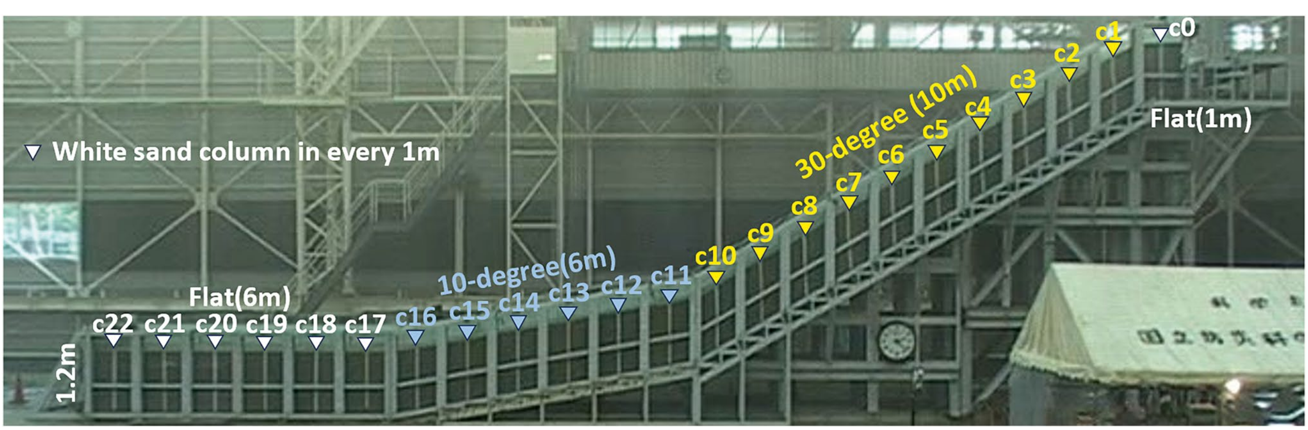

Fig. 27 Side view of the slope model (Case 2): White sand columns can be seen in each glass-paned section (between adjacent stiffeners)

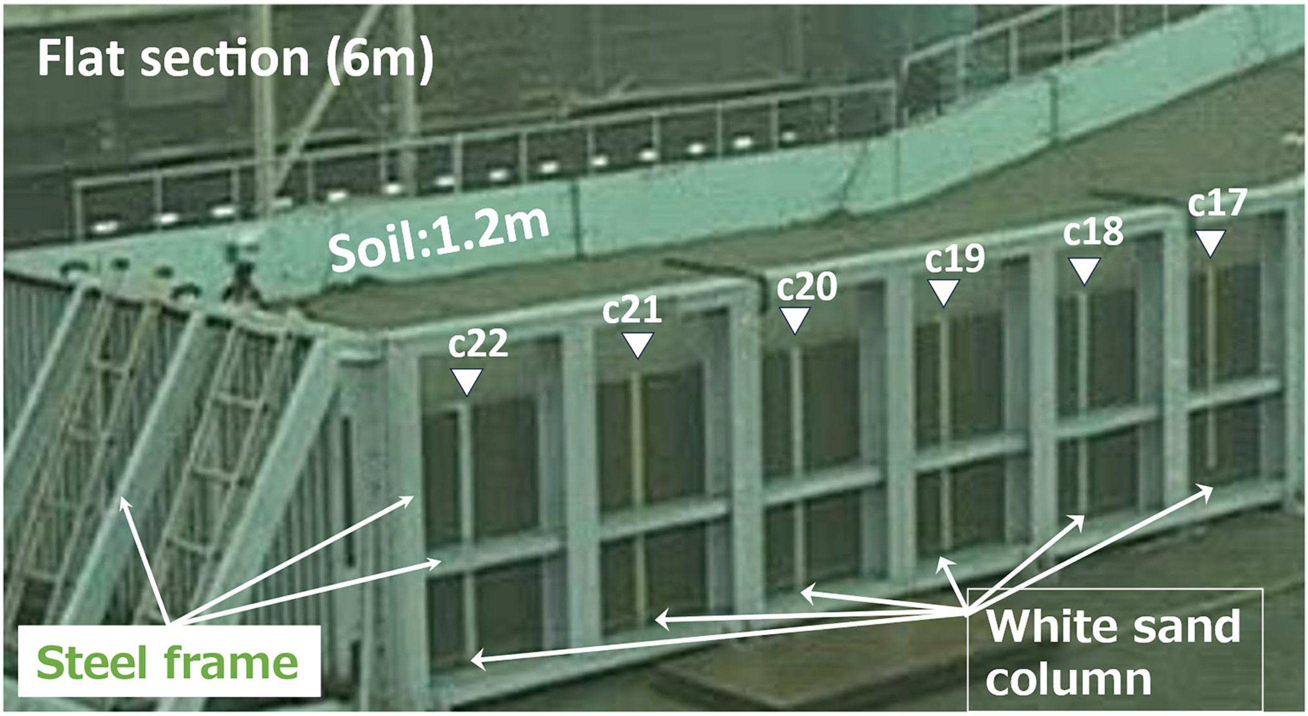

Fig. 28 Close-up of the soil bin's side wall

columns from C11 to C22 remained upright at this stage, showing neither deformation nor tilting. The observations above indicate that the slip surface was exclusively formed in the 30-degree slope area, and the collapse occurred within a one-second window between 8515s and 8516s. In Fig. 29 (3), kinks and bends further developed over the soil columns from c9 to c13, suggesting that a new slip surface was formed. On the other hand, the kinks of white sand columns shown in c6 to c9 show the earlier-developed slip surface, allowing the upper part of the landslide mass to move coherently over the 10-degree slope section. Fig. 29 (3) also shows an early sign of forming another new slip surface near the bottom of the soil bin over sand columns C13 to C15. This early sign developed into a new slip surface in Fig. 29 (4), shown as kinks of the sand columns from C14 to C17. At this stage, the soil mass that spread over the gentle 10-degree slope section has yet to stop moving, perhaps causing the new shear slip surfaces to develop within the undrained 10-degree slope section. Fig. 31 shows the frame-by-frame advance (three consecutive frames at every 1/6 s) of slope collapse taken from a video clip (30 frames/s) showing the whole process of the slip surface formation within the 30-degree slope section. The frame (1) at 8515.17 s in Fig. 31 shows that the sand columns, c1 through c10, developed bends and kinks. These bends and kinks show a slip surface geometry, which is shallower on both ends, including c1 and c2 near the top scar and c8 through c10 near the toe part. Bends and kinks are deep near the bottom of the soil bin at sand columns, c3 to c7, covering the middle part of the landslide mass. The trend is further developed in Fig. 31 (2) at 8515.51 s. The white sand columns c1 through c9 are entirely sheared off, resulting in columns c2 to c8 hiding behind upright steel stiffeners of the soil bin. The slip surface finally developed throughout its stretch in Fig. 31 (3) at 8515.34 s, while the other columns from c11 to c22 showed no remarkable change. Comparing these figures, we can discern that the initial stage of the entire collapse was marked by the appearance of transverse cracks at the top end of the 30-degree slope section (Fig. 29 Frame No. 1). This was associated with slight bends of white sand columns within the 30-degree slope section, as shown in

Fig. 29 Last 3-s swipe for frame-by-frame advance (at every 1-s interval) of the final entire collapse of the slope (Case 1)

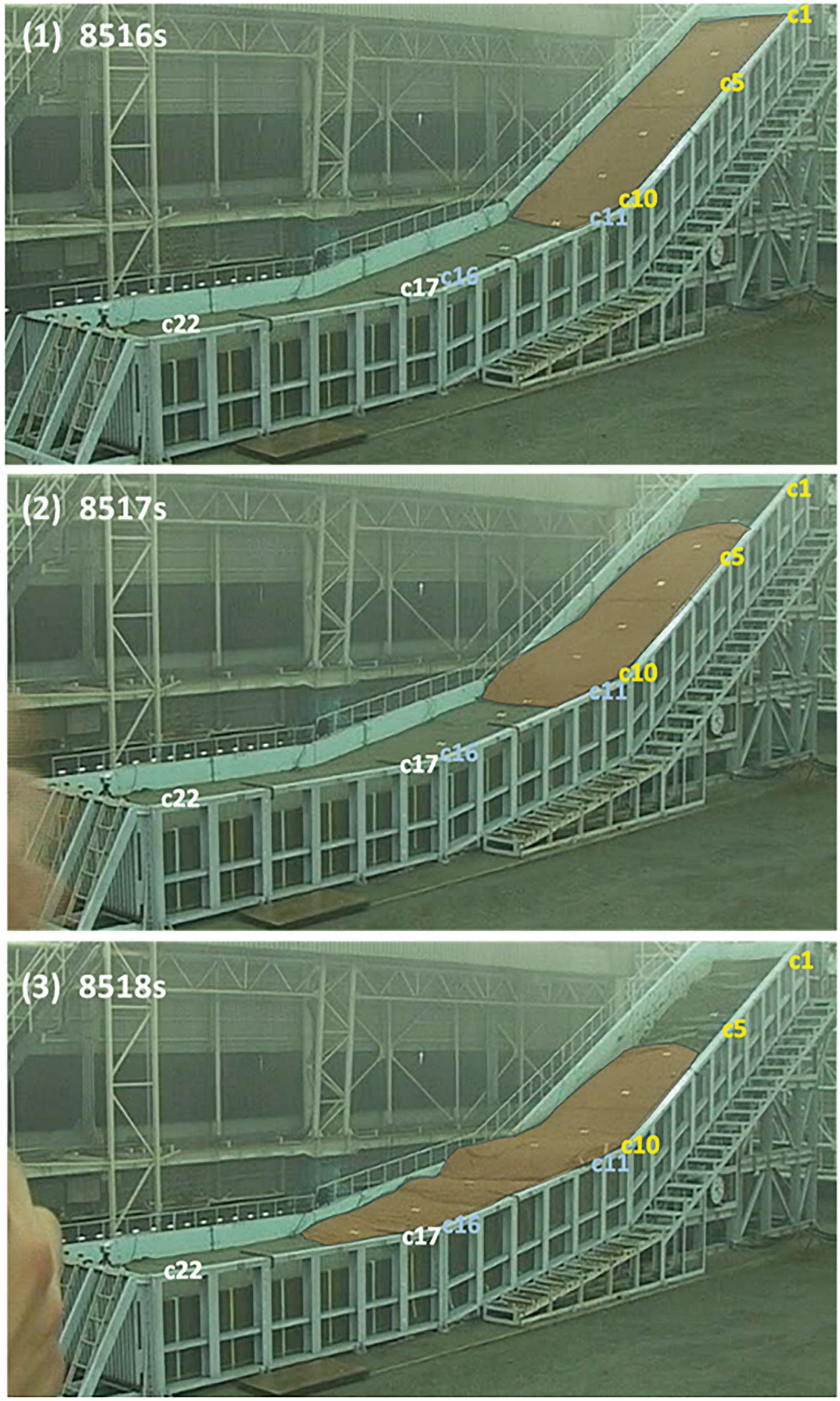

Fig. 30 Oblique views of the final stage of slope failure development (Case 1)

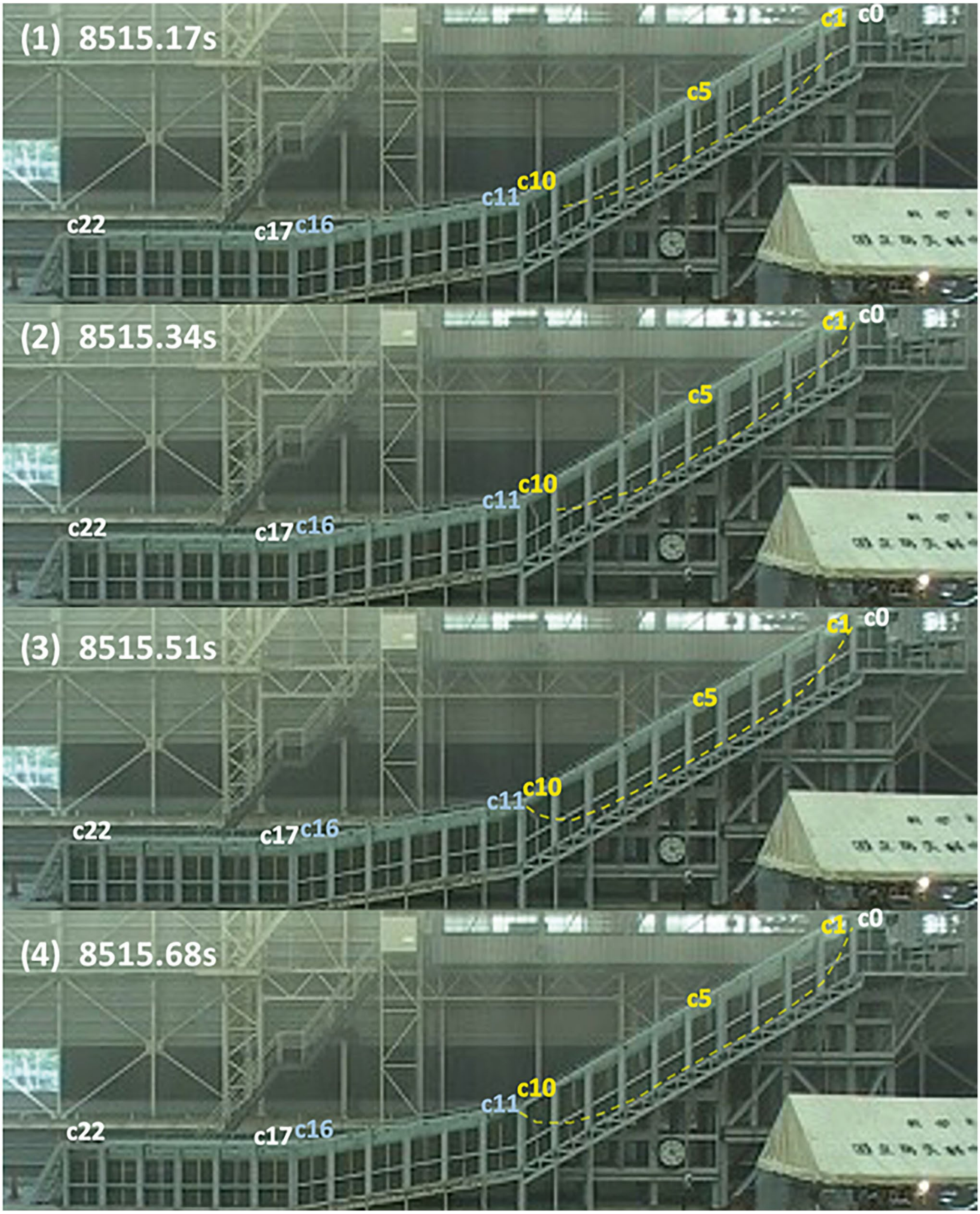

Fig. 31 final frame-by-frame collapse advance (5 frames at every 1/6-s interval, Case 1)

Frame No. 1 in Fig. 28. As time progressed, the appearance of kinks in sand columns indicated the development of a shear slip surface through the sandy soil only within the 30-degree slope section (Frame 2 in Fig. 28). This was associated with the formation of a bulge at the toe part of the 30-degree slope section (Frames 2 in Figs. 28 and 29). Finally, the toe part of the sliding soil mass overrode the gentler 10-degree slope section, entraining the surface part of the 10-degree slope section, thus causing two more shear bands (slip surfaces) to develop within the undrained 10-degree slope section. These findings have significant implications for our understanding of slope collapse dynamics.

5.2 Case 2 with Prior Rainfalls to the Main Rainfall Event

Likewise, as in Case 1, Fig. 32 shows the last 3-s swipe for frame-by-frame advance (at every 1-s interval) of the final entire collapse of the slope. This process is associated with cracking and bulging the model's surface at its top and toe parts, respectively, as shown in Fig. 33. The final frame-by-frame collapse advance (10 frames at every 1/3-s interval) is shown in Fig. 34.

5.3 Summary

Finally, Figs. 35 and 36 compare the developed slip surfaces and groundwater tables in Cases 1 and 2 to visualize better what is explained above.

Significant findings from the above experiments are:

1. The formation of a groundwater table plays a significant role in the soil deformation buildup, contributing to the destabilization and failure of the entire slope.
2. Water retention strongly influences the formation of the groundwater table in the slope's lower part, primarily affected by preceding rains.
3. When the toe part of a slope is soaked up with water, the downslope movement of the soil mass can cause the toe part's liquefaction, leading to faster collapse no matter how steep the slope is. Eventually, the landslide mass becomes more extensive, resulting in severe devastation.
4. Examining underground wet conditions is especially critical because rainfall infiltration and groundwater formation accelerate slope deformation.

6 Concluding Remarks

The large-scale rainfall simulator at the National Research Institute for Earth Science and Disaster Resilience (NIED) has the world's largest indoor rainfall area and sprinkling capacity, producing rainfall intensities between 15 and 300 mm/h. Its unique ability to control all experimental parameters is a crucial advantage, enabling the realization of more realistic natural rainfall conditions and external forces. This unique feature makes the experiments here invaluable, setting our research apart. However, it is crucial to stress the need for diverse simulation methods to exploit this advantage and fully encourage further research.

This article described the (1) outline of the facility, (2) experimental methods unique to large-scale models placed in the vast indoor rainfall area, and (3) experiment examples highlighting the importance of the preceding wetting process for large-scale models.

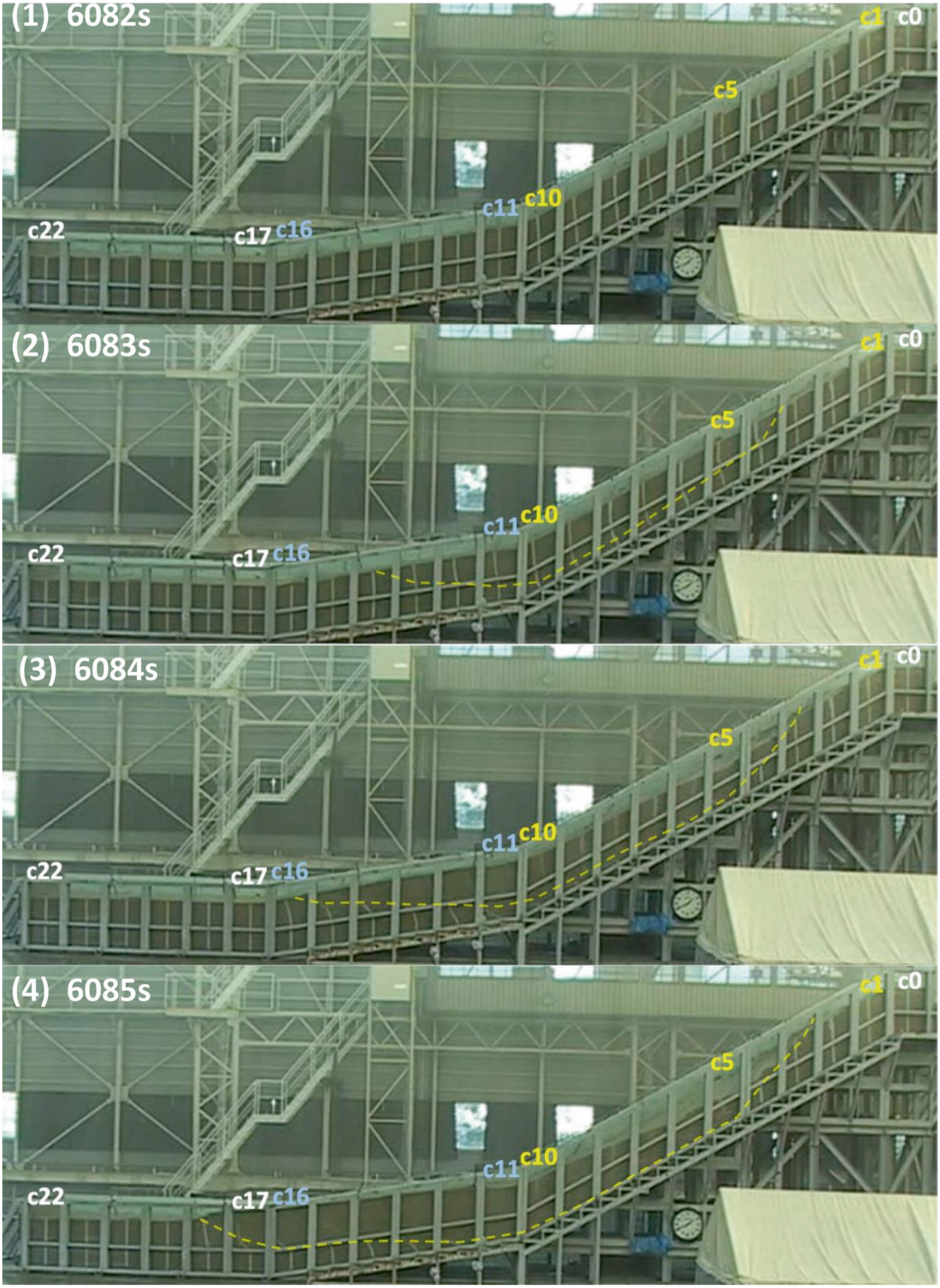

Fig. 32 Last 3-s swipe for frame-by-frame advance (at every 1-s interval) of the final entire collapse of the slope (Case 2)

Fig. 33 Oblique views of the final stage of slope failure development (Case 2)

The two experiment examples (Case 1 and Case 2) in this article are the same regarding the dimensions of the models prepared in a large soil bin, model materials, and compacting methods. The only difference is the pre-wetting process, which was given only in Case 2. The pre-wetting accelerated the model's soaking process remarkably, yielding a faster slope collapse.

The results of the large-scale model experiments showed that the slope ground becomes unstable due to rainfall with a change of a groundwater table. The results may serve as a benchmark test for improving the accuracy of ground deformation simulation due to rainfall infiltration and sediment flow simulation (debris flow) based on large deformation analysis using particle methods, and so on.

We will continue conducting various experiments to gain new insights into how experiments of this large-scale model are to be planned and share this knowledge worldwide.

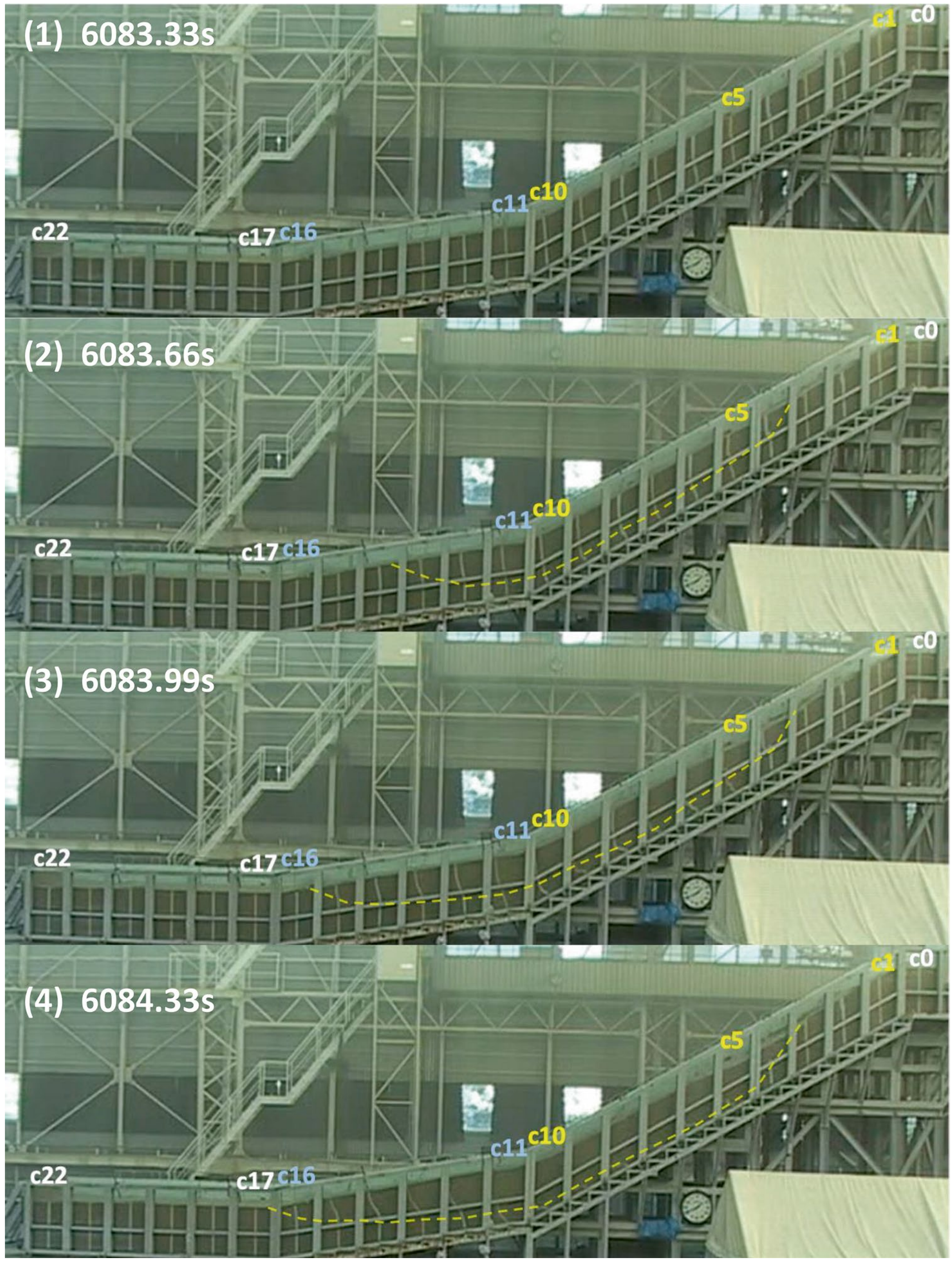

Fig. 34 Final frame-by-frame collapse advance (10 frames at every 1/3-s interval, Case 2)

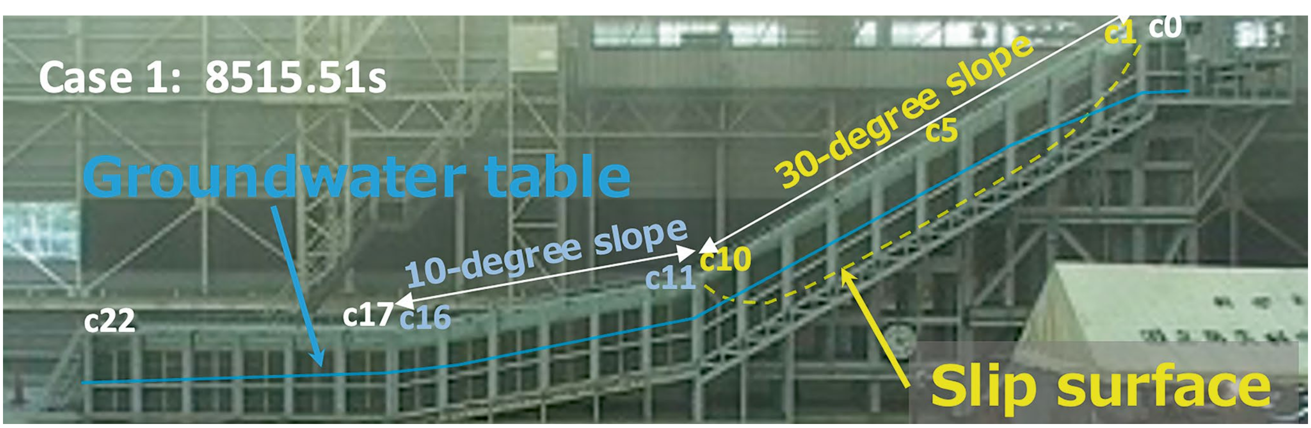

Fig. 35 Developed slip surface and groundwater table in Case 1

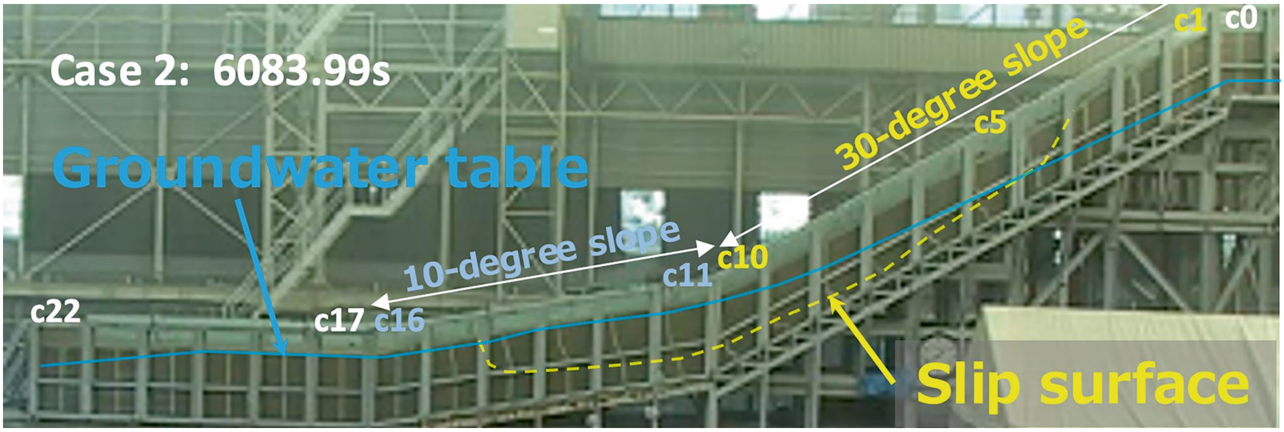

Fig. 36 Developed slip surface and groundwater table in Case 2

References

Fukuzono T (1985) A new method for predicting the failure time of a slope. In: Proceedings of the 4th international conference and field workshop on landslide, Japan landslide society, pp 145–150. Japan Landslide Society

Ishizawa T, Danjo T, Sakai N (2017) Real-time prediction method for slope failure caused by rainfall using slope monitoring records. J Disaster Res 12(5):980–992

Moriwaki H (1988) Current status and problems of slope failure research by model experiments. Geomorphology 9–4:255–268

Moriwaki H, Inokuchi T, Hattanji T, Sassa K, Ochiai H, Wang G (2004) Failure processes in a full-scale landslide experiment using a rainfall simulator. Landslides 1:277–288

Sakai N, Sakajo S (2008) Model tests of collapse of unsaturated slopes in rainfall. In: 10th International Symposium on Landslides and Engineered Slopes (Xi'an), pp 907–912

Sasahara K, Sakai N (2014) Development of shear deformation due to the increase of pore pressure in a sandy model slope during rainfall. Eng Geol 170:43–51

Sasahara K, Sakai N (2017) Shear and compression strain development in sandy model slope under repeated rainfall. Soils Found 57(6):920–934

Sasahara K, Sakai N, Kurihara J, Sun Y, Sakaue S (2007) Application of FEM analysis method to prediction of slope surface displacement and failure time due to rainfall infiltration. In: 42nd JSCE Conference

Take W, Bolton MD, Wong PCP, Yeung FJ (2004) Evaluation of landslide triggering mechanisms in model fill slopes. Landslide 1:173–184